AARHUS UNIVERSITY

Coversheet

This is the accepted manuscript (post-print version) of the article.
Contentwise, the accepted manuscript version is identical to the final published version, but there may be differences in typography and layout.

How to cite this publication
Please cite the final published version:

Publication metadata

PAPER

Cu$_8$GeSe$_6$-based thermoelectric materials with an argyrodite structure†

Binbin Jiang,[ab] Pengfei Qiu,[a] Espen Eikeland,[c] Hongyi Chen,[ab] Qingfeng Song,[ab] Dudi Ren,[a] Tiansong Zhang,[a] Jiong Yang,[d] Bo Brummerstedt Iversen,[c] Xun Shi*[a] and Lidong Chen*[ae]

Recently, liquid-like superionic thermoelectric materials have attracted great attention due to their extremely low lattice thermal conductivity and high thermoelectric figure of merit (*ZT*). Argyrodite-type compounds are typical superionic semiconductors with two independent structural units that can be used to separately tune electrical and thermal transport properties. In this work, we report that Cu$_8$GeSe$_6$ with an argyrodite structure is a new class of thermoelectric materials with extremely low lattice thermal conductivity. The presence of two independent structural units in Cu$_8$GeSe$_6$ provides the possibility of greatly improving its electrical transport properties while maintaining ultralow lattice thermal conductivity. By alloying Ag and Te in Cu$_8$GeSe$_6$, the *ZT* values are significantly improved to above unity at 800 K in Cu$_{7.6}$Ag$_{0.4}$GeSe$_{5.1}$Te$_{0.9}$, comparable with the best superionic liquid-like thermoelectric materials. The ultralow thermal conductivity is mainly attributed to the weak chemical bonding between Cu atoms and the rigid [GeSe$_6$] sublattice.

1. Introduction

Thermoelectric (TE) materials offer the possibility of directly converting industrial waste heat into electricity by using the Seebeck effect.[1–10] The energy conversion efficiency of a TE material is determined by the dimensionless TE figure of merit, $ZT = S^2\sigma T/\kappa$, where σ is the electrical conductivity, S is the Seebeck coefficient, κ is the thermal conductivity, and T is the absolute temperature. High TE performance in a material requires a large Seebeck coefficient to ensure a high voltage output, a high electrical conductivity to reduce the Joule heat, and a low thermal conductivity to maintain a temperature gradient between the material's hot side and cold side.[1–10]

However, simultaneously satisfying these requirements in one material is a very challenging task because σ, S, and κ are interrelated with each other. Improving one transport parameter is often accompanied by the deterioration of the others. Thus, good TE materials are expected to possess an ideal crystal structure with two independent structural units that can be used to separate the interrelation between electrical and thermal transport properties. Following this direction, in the past two decades, many new TE materials, *e.g.* filled-skutterudite,[11,12] clathrate,[13–15] and chalcopyrite-like compounds,[16,17] have been discovered and *ZT* values above unity have been reported.

Recently, superionic semiconductors have attracted great attention in the TE community because their crystal structures also have two independent structural units.[18,19] The anions in a superionic semiconductor usually form a rigid sublattice to maintain a crystalline solid. Likewise, the cations are mobile and kinetically distributed throughout the anion sublattice because there are lots of equilibrium positions with similar energies for cations leading to a "liquid-like" behavior. The rigid anion sublattice provides a crystalline pathway for carrier conduction, while the "liquid-like" cation sublattice strongly scatters phonons and even eliminates some of the transverse vibrational modes, leading to extremely low lattice thermal conductivities (κ_L). Such interesting electrical and thermal transport properties are well summarized by the "Phonon-Liquid Electron-Crystal" (PLEC) concept,[18,19] which can be regarded as the extension of the "Phonon-Glass Electron-Crystal" (PGEC) concept proposed by Slack.[20] Guided by the PLEC concept, low κ_L

^{a} State Key Laboratory of High Performance Ceramics and Superfine Microstructure, Shanghai Institute of Ceramics, Chinese Academy of Sciences, Shanghai 200050, China. E-mail: xshi@mail.sic.ac.cn, cld@mail.sic.ac.cn

^{b} University of Chinese Academy of Sciences, Beijing 100049, China

^{c} Center for Materials Crystallography, Department of Chemistry and iNANO, Aarhus University, DK-8000 Aarhus C, Denmark

^{d} Materials Genome Institute, Shanghai University, Shanghai 200444, China

^{e} Shanghai Institute of Materials Genome, Shanghai, China

† Electronic supplementary information (ESI) available: Calculations for the Grüneisen parameter, the parameters used to fit the heat capacity and lattice thermal conductivity, the temperature dependence of the heat capacity and XRD patterns, optical band gaps based on the measured diffuse reflectance spectrum, the results of the fitting for the heat capacity, the calculated band structure and total charge density map, chemical compositions and elemental maps. Crystallographic information files (CIF) for Cu$_8$GeSe$_6$ (ICSD #432278), Cu$_8$GeSe$_{5.1}$Te$_{0.9}$ (ICSD #432279) and Cu$_{7.6}$Ag$_{0.4}$GeSe$_{5.1}$Te$_{0.9}$. See DOI: 10.1039/c6tc05068a

This journal is © The Royal Society of Chemistry 2017

J. Mater. Chem. C, 2017, **5**, 943–952 | 943

values between 0.3 and 0.6 W m^{-1} K^{-1} and high ZT values between 1.0 and 2.1 have been observed in many superionic semiconductors, such as $Cu_{2-\delta}X$ (X = S, Se, Te),[18,19,21,22] $CuAgSe$,[23] $CuCrSe_2$,[24,25] and argyrodite-type compounds.[26–31] Among them, argyrodite-type compounds have a general formula $A_{(12-n)/m}^{m+}B^{n+}X_6^{2-}$, in which m and n are the valence states of A-cations (Li$^+$, Cu$^+$, Ag$^+$) and B-cations (Ga^{3+}, Si^{4+}, Ge^{4+}, Sn^{4+}, P^{5+}, As^{5+}), respectively, and X = S, Se or Te.[32] The crystal structures of argyrodite-type compounds at room temperature may be monoclinic, orthorhombic, hexagonal, or cubic, depending on the component elements. Nevertheless, at high temperatures, they usually crystallize in the high-symmetry cubic or hexagonal structure. In the high-temperature high-symmetry structures, the A-cations are mobile and disorderedly distributed inside the rigid sublattice formed by the B-cations and the X-anions.[33] Because of their high cation ionic conductivity, the study on argyrodites was mainly focused on applications as solid electrolytes in solid-state batteries.[34] The TE properties of argyrodite-type compounds have been measured very recently.[27] Extremely low κ_L values around 0.15–0.35 W m^{-1} K^{-1} and ZT values between 0.3 and 1.2 have been reported for Ag_8GeTe_6,[27,28] Ag_8SiTe_6,[29] Cu_7PSe_6,[35] and Ag_8SnSe_6.[26,30,31] These exciting results suggest that argyrodite-type materials are a new family of TE compounds. However, the high TE performance of argyrodite-type compounds has been rarely reported in Cu-based materials. In this study, we report a new Cu-based argyrodite-type compound Cu_8GeSe_6 with low κ_L values below 0.2 W m^{-1} K^{-1} and high ZT values above 1.0, suggesting Cu-based argyrodite-type compounds as a new class of TE materials.

2. Experimental and calculation details

High-purity raw elements, Cu (shots, 99.999%, Alfa Aesar), Ag (shots, 99.999%, Alfa Aesar), Ge (pieces, 99.999%, Alfa Aesar), Se (shots, 99.999%, Alfa Aesar), and Te (shots, 99.999%, Alfa Aesar), were weighed out in stoichiometric proportions and then sealed in silica tubes under vacuum. The tubes were heated to 1393 K and held at this temperature for 24 hours before quenching into cold water. Then, the quenched ingots were annealed at 873 K for 5 days. Finally, the products were ground into fine powder and sintered by Spark Plasma Sintering (Sumitomo SPS-2040) at 683–713 K under a pressure of 75 MPa for 5 minutes. High densities (>97% of the theoretical density) were obtained for all samples. The diameter of the pellets is 10 mm and the thickness is between 4 and 5 mm.

The phase purity and crystal structure were examined by single-crystal X-ray diffraction (SCXRD) and powder X-ray diffraction (PXRD). SCXRD experiments were performed on a SuperNova diffractometer from Agilent Technologies using Mo Kα radiation (λ = 0.71073 Å). Diffracted intensities were collected on a CCD detector, and the data were integrated and corrected for absorption using CrysAlisPro.[36] The structure solution and refinement were carried out with SHELXT using Olex2 gui.[37,38] PXRD experiments were performed on a Rigaku Rint 2000 diffractometer using Cu Kα radiation (λ = 1.5405 Å) at room temperature. The measurements

were performed between 10° and 160° with a scan width of 0.02° and a rate of 1° min^{-1}. Rietveld refinement was carried out using the FullProf Program Suite.[39]

Chemical compositions were estimated using energy dispersive spectrometry (EDS, OXDORD). Ten areas were randomly selected on each sample. The average compositions are listed in Table S1 (ESI†). Optical diffuse reflectance spectra of powder samples were obtained at room temperature using a Cary 5000 UV-Vis-NIR spectrometer equipped with an integrating sphere attachment and BaSO$_4$ as a reference. The data were collected in the range of 2400 to 600 nm at a scan rate of 600 nm min^{-1}. The electrical conductivity and the Seebeck coefficient were measured using an Ulvac ZEM-3 from 300 to 800 K. The thermal conductivity was calculated from $\kappa = DC_p\rho$, where the thermal diffusivity (D) was obtained by using a laser flash method (Netzsch LFA 457). The specific heat (C_p) was measured by differential scanning calorimetry (Netzsch DSC 404F3), and the density (ρ) was measured using the Archimedes method. The Hall coefficient (R_H) was measured using a Physical Property Measurement System (Quantum Design) by sweeping the magnetic field up to 3 T in both positive and negative field directions. The Hall carrier concentration (p_H) and the Hall mobility (μ_H) were estimated by $p_H = 1/eR_H$ and $\mu_H = \sigma R_H$, respectively. Heat capacities from 2.5 K to 300 K were measured utilizing the Heat Capacity option on Quantum Design PPMS. The mass for low temperature measurements was around 18 mg.

Lattice dynamics for Cu_8GeSe_6 was investigated with the frozen phonon method[40] as implemented in the Phonopy package.[41] We used the low-temperature structure of Cu_8GeSe_6 to run the calculations. The initial structure and atomic positions were taken from the reference.[42] A 1 × 1 × 1 unit cell (with 90 atoms in total) of the fully relaxed formula unit was constructed, and the Hellmann–Feynman forces were calculated by the DFPT method (density functional perturbation theory). A k-mesh of the 3 × 3 × 3 unit cell was used. The cut-off energy for the plane wave basis was set to 400 eV. After the phonon dispersion was obtained, the sound velocity for each acoustic phonon mode was calculated by averaging the zone-center velocities along different directions.

Density-functional theory (DFT) calculations were performed by using the Vienna Ab Initio Simulation Package (VASP) implemented with the projector-augmented wave (PAW) method.[43] Regular Monkhorst–Pack k-point meshes (where k is the electron wavevector) of 4 × 4 × 4 were used for self-consistent calculations with a cutoff energy of 400 eV and an energy convergence criterion of 10^{-6} eV. Electronic structure calculations were performed by using the Perdew–Becke–Ernzerhof (PBE) exchange correlation function. 6 eV for U was applied in Cu 3d states.[44]

3. Results and discussion

Single-crystal X-ray diffraction (SCXRD) measurements have been performed for Cu_8GeSe_6 at 100, 300 and 475 K. The crystallographic information is listed in Table 1. At low temperature, Cu_8GeSe_6 has a hexagonal structure (LT structure),

Table 1 Crystallographic information of Cu_8GeSe_6 and $Cu_8GeSe_{5.1}Te_{0.9}$

Sample	Cu_8GeSe_6 (LT)	Cu_8GeSe_6 (HT)	$Cu_8GeSe_{5.1}Te_{0.9}$
Chemical formula[a]	Cu_8GeSe_6	Cu_8GeSe_6	$Cu_{7.0(8)}GeSe_{5.3(1)}Te_{0.7(1)}$
Space group	$P6_3cm$; H	$P6_3mc$; H	$R3m$; H
Temperature/K	300	475	100
a/Å	12.6601(4)	7.284(13)	7.3196(5)
c/Å	11.7698(3)	11.920(12)	17.922(2)
Volume/Å^3	1633.71(11)	548(2)	831.58(15)
Z	6	2	3
ρ_{calc}/g cm^{-3}	6.545	6.006	6.143
μ/mm^{-1}	39.091	35.875	34.937
$F(000)$	2852	877	1355
$(\sin\theta/\lambda)_{max}$/Å^{-1}	0.67	0.63	0.63
$N_{Tot,obs}$	5620	1446	1887
$N_{Uniq,obs}$	1454	454	439
$N_{Parameters}$	79	55	53
GOF	1.211	1.102	1.248
R_{int}	0.058	0.071	0.096
R_1, $R_1[F^2 > 2\sigma(F^2)]$	0.044, 0.046	0.081, 0.090	0.056, 0.059
wR_2, $wR_2[F^2 > 2\sigma(F^2)]$	0.094, 0.096	0.209, 0.228	0.136, 0.139
$\Delta\rho_{max}$, $\Delta\rho_{min}$/e Å^{-3}	1.89, −4.77	2.37, −1.26	2.00, −1.74

[a] The partial atomic occupancies of Cu and the Te/Se ratio at two sites are free parameters in the structural model. Therefore, a slightly deviation in the composition is obtained compared with the predicted formula.

which is consistent with that reported by Jaulmes *et al.*[42] The space group is $P6_3cm$ and the cell parameters are a = 12.6601(4) Å and c = 11.7698(3) Å at 300 K. As depicted in Fig. 1, the anionic framework consists of two crystallographically distinct $[GeSe_4]^{-4}$ tetrahedra with one centered on a threefold rotation axis and the other on a 6_3 screw axis. In addition, two additional Se sites are located on mirror planes. All 5 Cu sites in the LT structure are fully occupied. Around 328 K, there is a phase transition (demonstrated by the DSC results in Fig. S1 and the PXRD patterns in Fig. S2, ESI†), resulting in a higher symmetry structure (HT structure) with the a- and b-axis shortened by a factor of $\sqrt{1/3} \sim 57.7\%$. The HT structure has the space group $P6_3mc$ with the cell parameters a = 7.284(13) Å and c = 11.920(12) Å at 475 K. $[GeSe_4]^{-4}$ tetrahedra in the HT structure are all crystallographically equivalent and centered on the 6_3 screw axis, while the two Se sites are located at the threefold rotation axis. Compared to the small changes in the anionic framework, the Cu atomic sites and their occupancies change significantly in the HT structure. The structure has five different Cu sites with the occupancies ranging from 0.14(3) to 0.59(4) at 450 K. This type of Cu atomic disorder is common in superionic semiconductors,[1,4] in which Cu ions can easily migrate among the partially occupied sites.
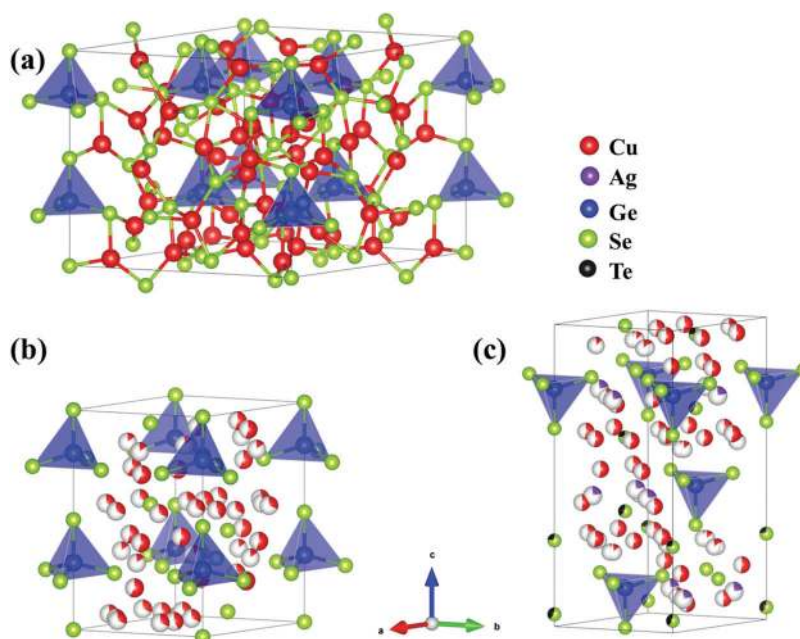

Fig. 1 (a) Low-temperature and (b) high-temperature crystal structures of Cu_8GeSe_6, and (c) crystal structure of $Cu_{7.6}Ag_{0.4}GeSe_{5.1}Te_{0.9}$. The atomic site occupancy is indicated by partial coloring of the atoms. The structure of $Cu_8GeSe_{5.1}Te_{0.9}$ can be visualized by replacing Ag with Cu.

SCXRD measurements have also been carried out for $Cu_8GeSe_{5.1}Te_{0.9}$ at 100 K and 300 K and the structure is shown in Fig. 1c, while the crystallographic information is listed in Table 1. Introducing a limited amount of Te into the anionic framework is found to completely change the crystal structure. All Cu positions in $Cu_8GeSe_{5.1}Te_{0.9}$ are disordered at 100 K. This new argyrodite-type compound shows a trigonal structure with the space group symmetry $R3m$ and cell parameters $a = 7.3196(5)$ Å and $c = 17.922(2)$ Å at 100 K. The structure is very similar to the HT structure of Cu_8GeSe_6 that also consists of $[GeSe_4]^{-4}$ tetrahedra and two separated Se sites, although the latter one now contain the substituted Te atoms. It is clear from the structural model that the Te atoms are substituted only at the separated Se sites rather than in the $[GeSe_4]^{-4}$ tetrahedra. This is consistent with the fact that Ge and Se can form a strong bond due to their significantly larger electronegativity difference. In contrast to the Cu_8GeSe_6 HT structure, the $[GeSe_4]^{-4}$ tetrahedra are not positioned as chains along the c-axis but are layered in an ABCABC fashion. The two separated Se/Te sites are located below and above the $[GeSe_4]^{-4}$ tetrahedra. The occupancies of the five heavily disordered Cu positions vary from 0.23(4) to 0.47(4). The structure of $Cu_8GeSe_{5.1}Te_{0.9}$ is very similar to the cubic argyrodite-type compounds Ag_8GeTe_6 and Ag_7TaS_6 which crystallize in the space group $F\bar{4}3m$ at room temperature.[45–47]

The measured powder diffractograms of $Cu_8GeSe_{5.1}Te_{0.9}$ and $Cu_{7.6}Ag_{0.4}GeSe_{5.1}Te_{0.9}$ are depicted in Fig. 2. All diffraction peaks are indexed by the new trigonal structures described above. The very similar diffractograms of these two samples suggest that further alloying of Ag into the structures has limited effect on the crystal symmetry. The $Cu_8GeSe_{5.1}Te_{0.9}$ structure obtained from the SCXRD data (at 300 K) was therefore used as a starting model for the Rietveld refinement of $Cu_{7.6}Ag_{0.4}GeSe_{5.1}Te_{0.9}$. The refined model parameters are given in Table 2. Due to the high degree of disorder in the Cu positions, the ADPs of the Cu atoms were constrained to have the values obtained from refinement of the SCXRD data (at 300 K). In $Cu_{7.6}Ag_{0.4}GeSe_{5.1}Te_{0.9}$ only one out of the five Cu positions has a significantly higher electron density compared with the $Cu_8GeSe_{5.1}Te_{0.9}$, indicating that Ag atoms are substituted into the structure only at this site. The large increase in electron density at this particular site further indicates that the site is solely occupied by the heavier Ag atoms.

In order to further understand the crystal structures, we performed microstructure characterization on Cu_8GeSe_6 and $Cu_8GeSe_{5.1}Te_{0.9}$ using high resolution transmission electron microscopy (HRTEM). As shown in Fig. 3, the HRTEM images and selected area electron diffraction (SAED) patterns clearly show that both Cu_8GeSe_6 and $Cu_8GeSe_{5.1}Te_{0.9}$ have high degrees of crystallinity. No obvious lattice distortions, dislocations, or amorphous phases are observed. The SAED patterns shown in Fig. 3c and f further support that Cu_8GeSe_6 and $Cu_8GeSe_{5.1}Te_{0.9}$ crystallize in hexagonal and trigonal structures, respectively, being consistent with the structures from SCXRD. Furthermore, based on the fast Fourier transformation (FFT) image shown in the inset of Fig. 3a, the [10-10] plane spacing $(d_{[10\text{-}10]})$ in hexagonal Cu_8GeSe_6 is calculated with a value of 11.08 Å,
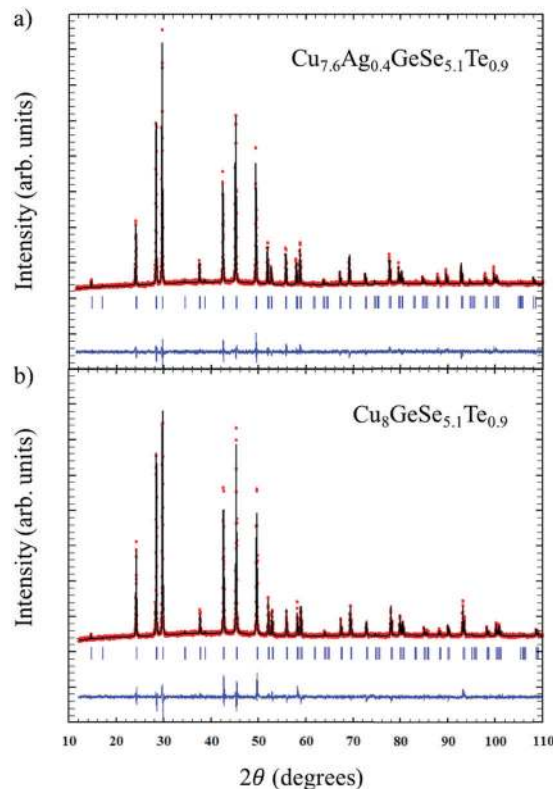

Fig. 2 Rietveld refinement of room temperature PXRD data for (a) $Cu_{7.6}Ag_{0.4}GeSe_{5.1}Te_{0.9}$ and (b) $Cu_8GeSe_{5.1}Te_{0.9}$. The red circles represent the measured intensity. The black lines are the intensities calculated from the trigonal structural model. The blue lines are the difference between experimental and calculated intensities. Vertical bars indicate Bragg positions.

Table 2 Refined parameters and quality factors based on the PXRD data for $Cu_8GeSe_{5.1}Te_{0.9}$ and $Cu_{7.6}Ag_{0.4}GeSe_{5.1}Te_{0.9}$ at room temperature

Nominal composition	Space group	a (Å)	c (Å)	R_p (%)	R_{wp} (%)	χ^2
$Cu_8GeSe_{5.1}Te_{0.9}$	$R3m$	7.34356(1)	17.9908(5)	5.30	4.15	1.51
$Cu_{7.6}Ag_{0.4}GeSe_{5.1}Te_{0.9}$	$R3m$	7.37156(7)	18.0582(3)	5.23	5.33	1.45

which is close to the value obtained from Rietveld refinement (10.95 Å, $d_{hkl} = \dfrac{1}{\sqrt{\dfrac{4}{3}\dfrac{(h^2 + hk + k^2)}{a^2} + \left(\dfrac{l}{c}\right)^2}}$). Similarly, the [1-10-4] plane spacing in $Cu_8GeSe_{5.1}Te_{0.9}$ is 3.65 Å, which is also consistent with the value (3.67 Å) obtained by Rietveld refinement.

The modification in the crystal structure induced by alloying Te in Cu_8GeSe_6 may change the coordination of the cations and subsequently affect the band gap (E_g). We estimated the optical band gaps of Cu_8GeSe_6, $Cu_8GeSe_{5.1}Te_{0.9}$, and $Cu_{7.6}Ag_{0.4}GeSe_{5.1}Te_{0.9}$ based on the measured diffuse reflectance spectrum (see Fig. S4, ESI†). E_g is calculated from the intercepts of the plots of $(\alpha h\nu)^2$ versus photon energy $h\nu$ based on the equation of $\alpha h\nu = \beta(h\nu - E_g)^n$,[48,49] where α is the absorption coefficient, $h\nu$ is the incident photon energy, β is the band tailing parameter, and n is the number associated with the type of electronic transition
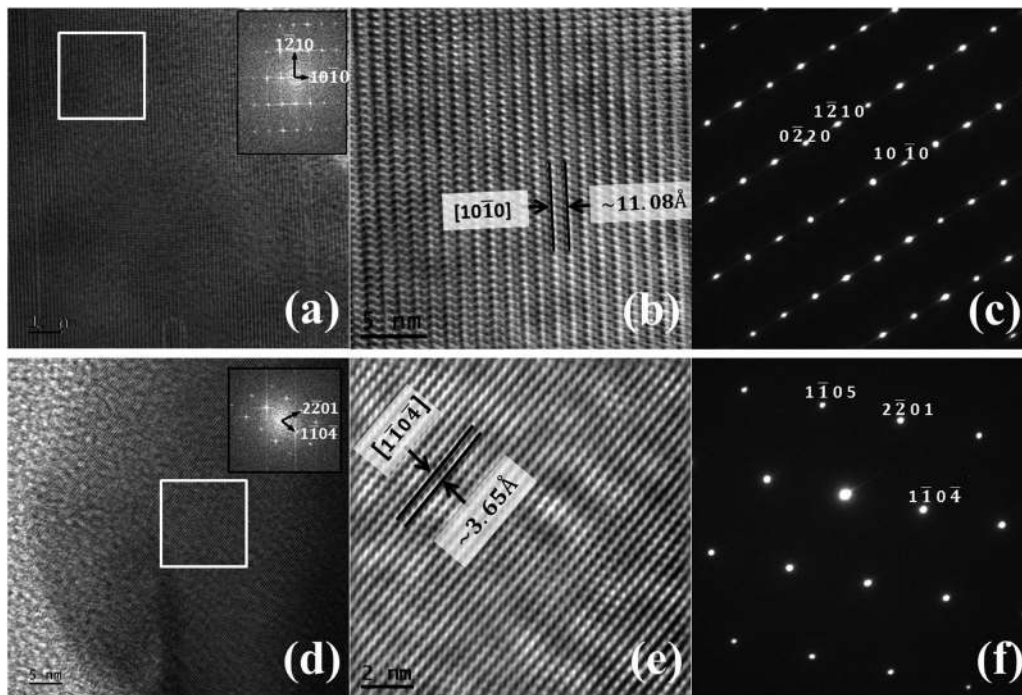
Fig. 3 Room temperature (a) high resolution transmission electron microscopy image, (b) inverse fast Fourier transformation image, and (c) selected area electron diffraction patterns of Cu_8GeSe_6. Room temperature (d) high resolution transmission electron microscope image, (e) inverse fast Fourier transformation image, and (f) selected area electron diffraction pattern of $Cu_8GeSe_{5.1}Te_{0.9}$. The inverse fast Fourier transformations were carried out in the boxed regions shown in (a) and (d). The selected area electron diffraction patterns shown in (c) and (f) were viewed along the [0001] and [11−20] zone axis, respectively.

($n = 1/2$ for direct allowed, $n = 2$ for indirect allowed, $n = 3/2$ for direct forbidden and $n = 3$ for indirect forbidden transitions). According to the calculated band structure shown in Fig. S5 (ESI†), we use $n = 1/2$ to calculate E_g. The E_g values for Cu_8GeSe_6 and $Cu_8GeSe_{5.1}Te_{0.9}$ are 1.08 eV and 0.71 eV, respectively, suggesting that the band gap is lowered in the Te-alloyed material. Likewise, $Cu_{7.6}Ag_{0.4}GeSe_{5.1}Te_{0.9}$ possesses a similar E_g value (0.76 eV) with $Cu_8GeSe_{5.1}Te_{0.9}$. This indicates that alloying a very small amount of Ag at Cu sites contributes weakly to the material's band gap. Thus, it is expected that the electrical transport properties of $Cu_{7.6}Ag_{0.4}GeSe_{5.1}Te_{0.9}$ might also be similar to that of $Cu_8GeSe_{5.1}Te_{0.9}$, which will be discussed below.

Fig. 4 shows the temperature dependences of the Seebeck coefficient (S), the electrical conductivity (σ), and the power factor ($S^2\sigma$) for Cu_8GeSe_6, $Cu_8GeSe_{5.1}Te_{0.9}$, and $Cu_{7.6}Ag_{0.4}GeSe_{5.1}Te_{0.9}$ above 300 K. All samples exhibit positive Seebeck coefficients, indicating that holes are the dominating carriers. In fact, almost all Cu-based TE compounds reported so far are p-type materials because of the presence of a very small amount of Cu vacancies introduced during the sample preparation processes. Due to the wide band gap ($E_g = 1.08$ eV), Cu_8GeSe_6 shows a quite large S value from 300 K to 750 K. The abnormal change in S around 350 K is attributed to the structure transition from the low-temperature phase to the high-temperature phase. The electrical conductivity for Cu_8GeSe_6 is very low at 300 K, but it quickly increases with increasing temperature, showing a typical semi-conducting behavior. At 750 K, σ is about three orders of magnitude higher than that at 300 K. Alloying Te at Se sites

significantly reduces S but enhances σ throughout the entire measured temperature range. At 300 K, the σ for $Cu_8GeSe_{5.1}Te_{0.9}$ is four orders of magnitude higher than that for Cu_8GeSe_6. Notably, the σ in $Cu_8GeSe_{5.1}Te_{0.9}$ decreases with increasing temperature, showing a metallic-like behavior instead of the semiconducting behavior in Cu_8GeSe_6. Such increased electrical conductivity in $Cu_8GeSe_{5.1}Te_{0.9}$ is mainly attributed to the increased hole concentrations (see Table 3). Because the electro-negativity of Te ($\chi_p = 2.10$) is smaller than those of Se ($\chi_p = 2.55$) or S ($\chi_p = 2.58$), the chemical bonds between Cu and Te should be weaker than those between Cu and Se or Cu and S. Thus, Cu vacancies are more easily generated in the Cu–Te based compounds. A similar phenomenon has also been observed in Cu_2X (X = S, Se, Te) liquid-like materials, in which Cu_2Te always possesses many Cu vacancies and high σ compared with Cu_2S and Cu_2Se.[18,19,21,22] Because Ag has the same outermost electron number as Cu, the electrical transport properties of $Cu_8GeSe_{5.1}Te_{0.9}$ and $Cu_{7.6}Ag_{0.4}GeSe_{5.1}Te_{0.9}$ are quite similar (see Fig. 4a and b). Moreover, different from Cu_8GeSe_6, both S and σ in $Cu_8GeSe_{5.1}Te_{0.9}$ and $Cu_{7.6}Ag_{0.4}GeSe_{5.1}Te_{0.9}$ show a smooth curve from 300 K to 800 K since there is no structural transition in these two materials. Based on the measured S and σ, the power factors (PF = $S^2\sigma$) are calculated and plotted in Fig. 4c. The PF value for Cu_8GeSe_6 is small in the whole temperature range because of the low σ. After alloying Te at Se sites, σ is greatly enhanced and thus PF is significantly increased to about 2 $\mu W\ cm^{-1}\ K^{-2}$ at 300 K and 6 $\mu W\ cm^{-1}\ K^{-2}$ at 800 K. Alloying Ag at Cu sites scarcely affects the electrical transport properties,
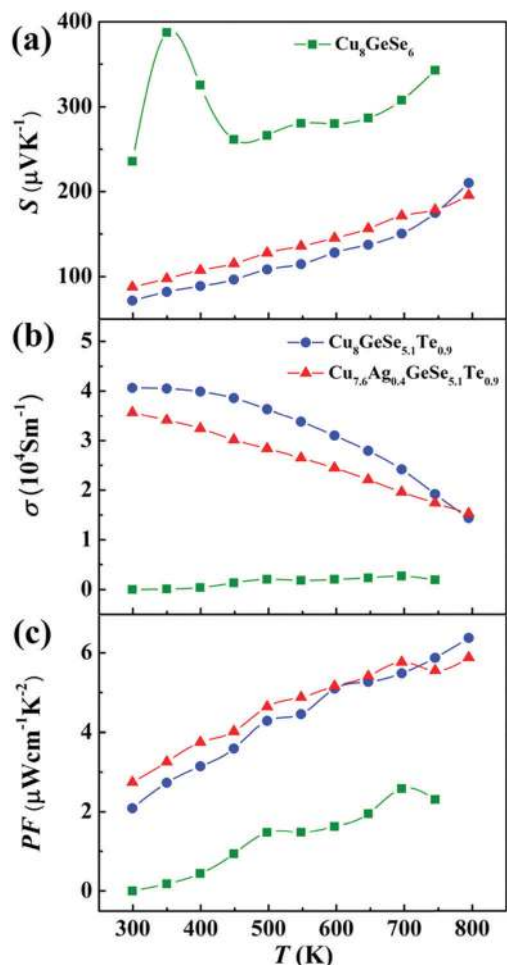
Fig. 4 Temperature dependences of (a) Seebeck coefficient (S), (b) electrical conductivity (σ), and (c) power factor (PF) for Cu_8GeSe_6, $Cu_8GeSe_{5.1}Te_{0.9}$, and $Cu_{7.6}Ag_{0.4}GeSe_{5.1}Te_{0.9}$.

Table 3 Room temperature electrical conductivity (σ), Seebeck coefficient (S), Hall carrier concentration (p_H), Hall mobility (μ_H), lattice thermal conductivity (κ_L), and Debye temperature (Θ_D) of Cu_8GeSe_6, $Cu_8GeSe_{5.1}Te_{0.9}$ and $Cu_{7.6}Ag_{0.4}GeSe_{5.1}Te_{0.9}$. The average speed of sound (ν_{avg}) of Cu_8GeSe_6 reported by Li et al.[31] is also listed

Composition	Cu_8GeSe_6	$Cu_8GeSe_{5.1}Te_{0.9}$	$Cu_{7.6}Ag_{0.4}GeSe_{5.1}Te_{0.9}$
σ (10^4 S m^{-1})	0.0003	4.1	3.6
S (μV K^{-1})	236	72	88
p_H (10^{20} cm^{-3})	0.009	3.8	3.3
μ_H (cm^2 V^{-1} s^{-1})	0.23	6.11	6.77
Θ_D (K)	302.81	297.3	288.83
ν_{avg} (m s^{-1})[31]	1793	—	—
κ_L (W m^{-1} K^{-1})	0.31	0.41	0.20

thus $Cu_{7.6}Ag_{0.4}GeSe_{5.1}Te_{0.9}$ shows similar PF values to $Cu_8GeSe_{5.1}Te_{0.9}$. These PF values are comparable with the best superionic conductors reported so far such as $Cu_{2-\delta}X$ (X = S, Se, and Te),[18,19,21,22] $CuCrSe_2$,[25] Ag_8SnSe_6,[26,30,31] etc.

Fig. 5a shows the thermal conductivity (κ) of Cu_8GeSe_6, $Cu_8GeSe_{5.1}Te_{0.9}$, and $Cu_{7.6}Ag_{0.4}GeSe_{5.1}Te_{0.9}$. As expected, all samples demonstrate low κ values of less than 1 W m^{-1} K^{-1} in the whole temperature range. The total κ in a solid includes

two parts. One is the carrier part (κ_c), which can be calculated by the Wiedemann–Franz law ($\kappa_c = LT\sigma$, where L is the Lorenz number, $L = 2.0 \times 10^{-8}$ V^2 K^{-2}).[18] The other one is the lattice part (κ_L), which is obtained by subtracting κ_c from the total κ. Fig. 5b presents κ_L for these three samples together with some typical TE materials. κ_L for Cu_8GeSe_6 is only about 0.2–0.3 W m^{-1} K^{-1}, which is among the lowest values in all TE materials reported so far. After alloying Te at the Se sites, the κ_L in $Cu_8GeSe_{5.1}Te_{0.9}$ is slightly increased as compared with that in Cu_8GeSe_6, and this may be linked to the changes in the crystal structures as shown above. However, the κ_L value is still very low and only around 0.4 W m^{-1} K^{-1}. Further alloying of Ag in $Cu_8GeSe_{5.1}Te_{0.9}$ seems to reduce κ_L down to 0.2 W m^{-1} K^{-1}, as shown in Fig. 5b. Due to the atomic mass and radius differences between Ag and Cu, doping Ag at the Cu sites introduces more point defects to scatter phonons and consequently this further reduces κ_L. Considering the similar electrical properties between $Cu_8GeSe_{5.1}Te_{0.9}$ and $Cu_{7.6}Ag_{0.4}GeSe_{5.1}Te_{0.9}$ shown in Fig. 4, it is strongly suggested that the thermal transport properties of argyrodite-type compounds can be independently tuned without significantly changing the electrical transport properties. This observation is similar to previous studies of element-alloyed thermoelectric materials.

The extremely low κ_L values in Cu_8GeSe_6-based compounds are believed to be caused by the weak chemical bonding between the Cu ions and the rigid [GeSe$_6$] sublattice. In the high-temperature superionic phase, the randomly distributed Cu ions are weakly bonded inside the [GeSe$_6$] sublattice exhibiting the liquid-like behavior, which can strongly scatter phonons and lower κ_L. In the low-temperature phase, although the Cu-ion sites are ordered, the weak chemical bonding still exists, which would lead to very strong atomic vibrational anharmonicity and also significantly disrupt heat propagation. We calculated the total charge density distribution of Cu_8GeSe_6 and plotted the map as shown in Fig. S6 (ESI†). Clearly, the chemical bonding between Cu and Se, especially that between Cu5 and Se3, is much weaker than that between Ge and Se (see the marked bond between Ge2 and Se5 in Fig. S6, ESI†). Such weak chemical bonding is aroused by the longer interatomic distance between Cu5 and Se3, about 2.93 Å, as shown in Fig. S6 (ESI†). The presence of this weak chemical bonding in both the low-temperature and high-temperature phases would lead to the ultralow lattice thermal conductivity in a wide temperature range for liquid-like materials with very weak temperature dependence.[1] In this study, the observed κ_L values are completely consistent with this general trend (see Fig. 5b). We calculated the Grüneisen parameter (γ) for Cu_8GeSe_6 since γ reflects the lattice vibrational anharmonicity. The calculation details are shown in the ESI.† As expected, we obtain an extremely high γ value, about 3.7, in Cu_8GeSe_6, which is much higher than most of the state-of-the-art TE materials ($\gamma = 1.0$–2.5).[52] In fact, except for the liquid-like materials, similar high γ values have only been observed in a few TE materials such as SnSe ($\gamma = 4.1$ in a axes) and $AgSbSe_2$ ($\gamma = 3.5$), which also have very low κ_L values.[53,54] The greatly disrupted heat propagation due to the weak chemical bonding between the Cu ions and the rigid [GeSe$_6$] sublattice can
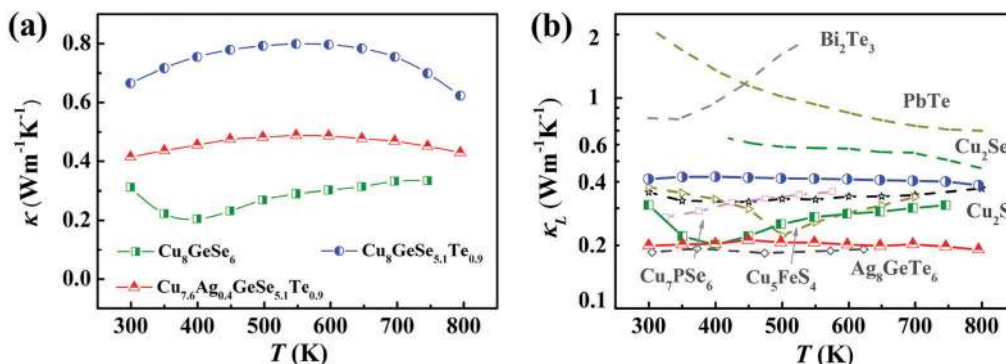
Fig. 5 Temperature dependences of (a) thermal conductivity (κ) and (b) lattice thermal conductivity (κ_L) for Cu_8GeSe_6, $Cu_8GeSe_{5.1}Te_{0.9}$, and $Cu_{7.6}Ag_{0.4}GeSe_{5.1}Te_{0.9}$. The lattice thermal conductivities of some typical TE materials (PbTe,[5] Bi_2Te_3,[50] Cu_2Se,[18] Cu_2S,[19] Ag_8GeTe_6,[28] Cu_7PSe_6,[35] and Cu_5FeS_4[51]) are included for comparison.

also be ascertained by the extremely low average sound velocity (ν_{avg}) and the phonon mean free path (l) in Cu_8GeSe_6. The average sound velocity of the low-temperature Cu_8GeSe_6 phase is only 1793 m s^{-1},[31] which is even lower than those observed in binary superionic conductors such as Cu_2Se (ν_{avg} = 2393 m s^{-1})[13] and Cu_2S (ν_{avg} = 2663 m s^{-1}).[19] Using this average sound velocity, we further calculated the phonon mean free path (l) by using the relationship $\kappa_L = C_v\nu_{avg}l/3$, where C_v is the heat capacity at constant volume.[31] Under the hypothesis that the heat capacity at constant volume (C_v) is equal to the heat capacity at constant pressure (C_p), a very small l of about 2.1 Å at 300 K is obtained, which is very close to the shortest atomic distance in the low-temperature hexagonal phase (2.3 Å between the nearest Ge and Se atoms reported by Jaulmes[42]). Similarly, the phonon mean free path in $Cu_8GeSe_{5.1}Te_{0.9}$ is also calculated. Here the l value is 2.8 Å, which is also comparable with the shortest atomic distance in the cubic $Cu_8GeSe_{5.1}Te_{0.9}$ phase (2.3 Å).

Generally, weak chemical bonding can lead to the presence of low-lying phonon modes, which can be approximately described as an Einstein mode with a characteristic temperature of Θ_E. We have measured the low-temperature heat capacity of Cu_8GeSe_6 and fitted the C_p data with one Debye

mode and two Einstein modes according to the following equation:[55]

$$\frac{C_p}{T}(x) = \varphi + \beta x + A\Theta_{E1}^2 x^{-\left(\frac{3}{2}\right)} \frac{e^{\frac{\Theta_{E1}}{\sqrt{x}}}}{\left(e^{\frac{\Theta_{E1}}{\sqrt{x}}} - 1\right)^2} + B\Theta_{E2}^2 x^{-\left(\frac{3}{2}\right)} \frac{e^{\frac{\Theta_{E2}}{\sqrt{x}}}}{\left(e^{\frac{\Theta_{E2}}{\sqrt{x}}} - 1\right)^2}, \quad (1)$$

where x represents T^2, φ is the electronic contribution to the heat capacity, Θ_{E1} and Θ_{E2} are the Einstein temperatures of the two local vibrational modes, and A and B are constants. The fitted curves with those parameters are presented in Table S2 (ESI†) and Fig. 6a. Two Θ_E values, 36.4 ± 0.4 K and 82.1 ± 0.9 K, are obtained, corresponding to the presence of two Einstein oscillators with low energies of 3.1 meV and 7.1 meV, respectively. Similar low-energy Einstein oscillators have been observed in cage-like compounds (e.g. skutterudites,[56,57] and clathrates[58]) and other liquid-like materials such as Cu_2Se.[59] These low-energy Einstein oscillators suggest the presence of low-lying
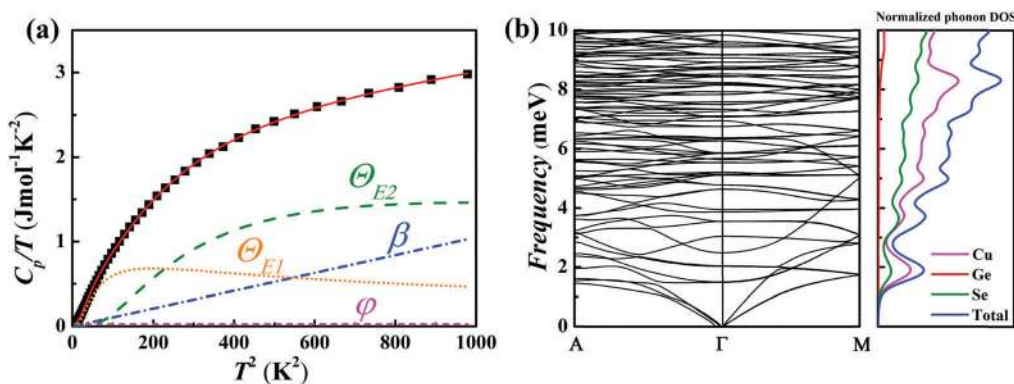

Fig. 6 (a) Measured C_p/T versus T^2 for Cu_8GeSe_6 (black squires). The red solid line represents the fitted curve by using one Debye mode and two Einstein modes. The other lines represent the electronic term φ, Debye term β, and two Einstein terms, Θ_{E1} and Θ_{E2}, respectively. (b) Room temperature phonon dispersion relations for Cu_8GeSe_6 (left picture) and total and partial phonon density of states (right picture).

optical phonon modes located in the very low-frequency range in the phonon spectra. This is further confirmed by our calculated phonon dispersion curve shown in Fig. 6b. The low-energy optical phonon mode at the Γ point starts from about 2 meV, comparable with the lowest Einstein oscillator shown above. This value is much lower than that in the filled skutterudites (about 5 meV)[55] and comparable with that in Cu_2Se (about 3 meV).[59] The optical phonon modes are dispersionless and very flat, and thus they barely contribute to the heat transport properties due to their very small phonon group velocity. Furthermore, they have strong interactions with the acoustic phonons to block heat transfer. The total and partial phonon density of states (PDOS) are plotted in Fig. 6b. At a low-frequency range, the total PDOS is mainly contributed by Cu atoms, further confirming the weak chemical bonding between the Cu atoms and the rigid $[GeSe_6]$ sublattice. We also calculated the average sound velocity and obtained a value of 1783 m s^{-1} consistent with the experimental value of 1793 m s^{-1}.[31] To sum up, the low-frequency optical phonon modes induced by the Cu atoms, as well as the ultralow sound velocity, contribute to the extremely low lattice thermal conductivity in Cu_8GeSe_6-based argyrodite-type compounds.

Similar to Cu_8GeSe_6, two low-energy Einstein oscillator modes in $Cu_8GeSe_{5.1}Te_{0.9}$ and $Cu_{7.6}Ag_{0.4}GeSe_{5.1}Te_{0.9}$ have also been obtained by modelling the C_p data, as shown in the ESI† (see Table S2 and Fig. S7). Therefore, strong phonon resonant scattering is also expected in these Cu_8GeSe_6-based compounds. In addition, the dopants can introduce more point defects to strengthen the scattering of high-frequency phonons and thus make the system more complex. In order to further understand the ultralow κ_L in these doped compounds, we modeled the low-temperature κ_L data of $Cu_{7.6}Ag_{0.4}GeSe_{5.1}Te_{0.9}$ using the Callaway model:[60,61]

$$\kappa_L = \frac{k_B}{2\pi^2 v_{avg}}\left(\frac{k_B T}{\hbar}\right)^3 \int_0^{\theta_D/T} \frac{x^4 e^x}{\tau_C^{-1}(e^x-1)^2}dx, \quad (2)$$

where $x = \hbar\omega/k_B T$ is the reduced phonon frequency, ω is the phonon frequency, k_B is the Boltzmann constant, $\hbar$ is the reduced Planck's constant, θ_D is the Debye temperature, and τ_C is the overall phonon scattering relaxation time. Four phonon scattering mechanisms are considered here, including phonon–phonon Umklapp scattering (U), grain boundary scattering (B), point defect scattering (PD), and phonon resonant scattering (RES). The overall phonon scattering relaxation time is expressed as[61]

$$\tau_C^{-1} = \frac{v_{avg}}{L} + A\omega^4 + B\omega^2 T e^{-\theta_D/3T} + \sum \frac{C_i\omega^2}{(\omega_i^2-\omega^2)^2}, \quad (3)$$

where L is the grain size; ω_i ($i = 1$ and 2) is the resonant frequency; and A, B and C_i ($i = 1$ and 2) are the fitting parameters for point defect scattering, phonon–phonon Umklapp scattering, and phonon resonant scattering, respectively. The fit is excellent with $R^2 = 0.99800$ and $\chi^2 = 0.005987$. The contributions from various phonon scattering mechanisms to the total κ_L are plotted in Fig. 7a. The grain boundaries greatly suppress κ_L at low temperature, while its effect can be neglected above 50 K. When the point defect and phonon resonant scatterings are involved, a good agreement between the experimental data and calculated curve is obtained. The resonant frequencies obtained by fitting the low temperature κ_L are 2.3 meV and 4.5 meV, comparable with the values obtained by fitting the C_p data (see Table S4, ESI†). As expected, the effect of point defect scattering on κ_L reduction is very strong in $Cu_{7.6}Ag_{0.4}GeSe_{5.1}Te_{0.9}$, because Ag/Te dopants have large atomic mass and radius differences from the host atoms to provide strong mass and strain field fluctuation phonon scatterings. This can be confirmed by the spectral lattice thermal conductivity (κ_s) calculated by[62]

$$\kappa_s = \frac{k_B}{2\pi^2 v_{avg}}\left(\frac{k_B T}{\hbar}\right)^3 \frac{x^4 e^x}{\tau_t^{-1}(e^x-1)^2}, \quad (4)$$

where τ_t is the phonon scattering relaxation time including various scattering mechanisms, termed U, U + B, U + B + PD, U + B + PD + RES. Fig. 7b shows the calculated κ_s at 300 K based on the fitting parameters shown in Table S4 (ESI†). According to the Callaway model, κ_L is proportional to the areas under the curves. Clearly, grain boundary scattering (Area I) and phonon resonant scattering (Area III) mainly affect the low-frequency phonons, while point defect scattering (Area II) predominantly interrupts the high-frequency phonon transfer. By combining
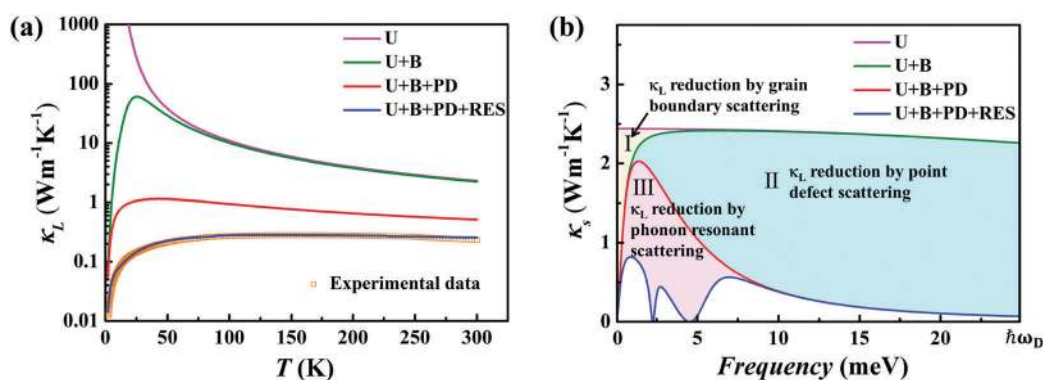

Fig. 7 (a) Contributions from various phonon scattering mechanisms to the lattice thermal conductivity (κ_L) in $Cu_{7.6}Ag_{0.4}GeSe_{5.1}Te_{0.9}$. U, B, PD, and RES denote the phonon–phonon Umklapp process, grain boundary scattering, point defect scattering, and phonon resonant scattering, respectively. (b) Calculated spectral thermal conductivities (κ_s) for $Cu_{7.6}Ag_{0.4}GeSe_{5.1}Te_{0.9}$ at 300 K.
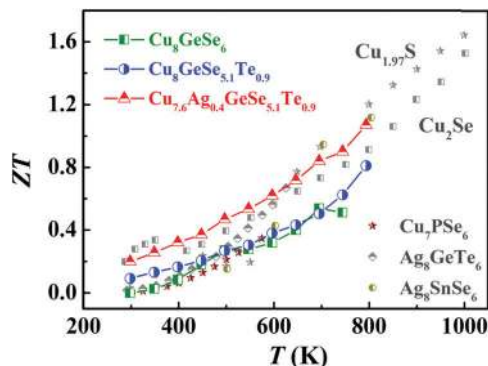
Fig. 8 Temperature dependence of the TE dimensionless figure of merit for Cu_8GeSe_6, $Cu_8GeSe_{5.1}Te_{0.9}$, and $Cu_{7.6}Ag_{0.4}GeSe_{5.1}Te_{0.9}$. The ZT data for some argyrodite-type compounds (Ag_8SnSe_6,[26] Ag_8GeTe_6,[28] Cu_7PSe_6[35]) and copper chalcogenides (Cu_2Se,[18] $Cu_{1.97}S$[19]) are included for comparison.

these phonon scattering mechanisms, the ultralow κ_L, about 0.2 W m^{-1} K^{-1}, is obtained in $Cu_{7.6}Ag_{0.4}GeSe_{5.1}Te_{0.9}$, as shown in Fig. 5b.

As mentioned above, the presence of two independent structural units in argyrodite-type compounds provides the possibility of simultaneously realizing good electrical transport properties and low thermal conductivity, which clearly would lead to good TE properties. Fig. 8 illustrates the temperature dependence of the TE dimensionless figure of merit (ZT) for Cu_8GeSe_6, $Cu_8GeSe_{5.1}Te_{0.9}$, and $Cu_{7.6}Ag_{0.4}GeSe_{5.1}Te_{0.9}$. The ZT data for some other argyrodite-type compounds and copper chalcogenides are also included for comparison. Although the electrical transport properties of Cu_8GeSe_6 are not very high, a peak ZT of 0.5 at 750 K is obtained due to the extremely low κ_L values. Alloying with Te and Ag greatly improves the electrical properties while maintaining the ultralow lattice thermal conductivity, and the ZT values are correspondingly improved in the whole temperature range with a maximum value above 1.0 at 800 K in $Cu_{7.6}Ag_{0.4}GeSe_{5.1}Te_{0.9}$. Similar to other liquid-like superionic thermoelectric materials, the stability of Cu_8GeSe_6 during actual application may not be as good as in classical thermoelectric materials. The copper precipitates at high currents and temperature gradients might lead to the degradation of the thermoelectric properties.[63,64] However, as basic research, our work is helpful for understanding many fundamental questions about the liquid-like thermoelectric materials, for example the ultralow lattice thermal conductivity and high thermoelectric performance.

4. Conclusion

In this study, guided by the PLEC concept, a new Cu-based argyrodite-type TE compound Cu_8GeSe_6 is reported. A maximum ZT of 0.5 at 750 K is achieved in the Cu_8GeSe_6 matrix due to its ultralow lattice thermal conductivity that is related to the weak chemical bonding between the Cu ions and the [$GeSe_6$] sublattice. By alloying Te and Ag in the two independent structural units in Cu_8GeSe_6, its electrical transport properties were greatly improved

throughout the entire measured temperature range, while the extremely low lattice thermal conductivity is maintained. Consequently, the ZT values are significantly improved in $Cu_{7.6}Ag_{0.4}GeSe_{5.1}Te_{0.9}$, with a maximum value above unity at 800 K.

Author contributions

B. B. J., P. F. Q. and X. S. designed the research; B. B. J., E. E., Q. F. S., D. D. R. and T. S. Z. performed the experiments; H. Y. C. and J. Y. did the calculation; B. B. J., P. F. Q., E. E., B. B. I., X. S. and L. D. C. wrote the paper.

Acknowledgements

References

1 X. Shi, L. D. Chen and C. Uher, *Int. Mater. Rev.*, 2016, **61**, 379–415.

2 M. Zebarjadi, K. Esfarjani, M. S. Dresselhaus, Z. F. Ren and G. Chen, *Energy Environ. Sci.*, 2012, **5**, 5147–5162.

3 R. J. Mehta, Y. L. Zhang, C. Karthik, B. Singh, R. W. Siegel, T. Borca-Tasciuc and G. Ramanath, *Nat. Mater.*, 2012, **11**, 233–240.

4 P. F. Qiu, X. Shi and L. D. Chen, *Energy Storage Mater.*, 2016, **3**, 85–97.

5 Y. Z. Pei, X. Y. Shi, A. LaLonde, H. Wang, L. D. Chen and G. J. Snyder, *Nature*, 2011, **473**, 66–69.

6 J. P. Heremans, V. Jovovic, E. S. Toberer, A. Saramat, K. Kurosaki, A. Charoenphakdee, S. Yamanaka and G. J. Snyder, *Science*, 2008, **321**, 554–557.

7 X. Shi and L. D. Chen, *Nat. Mater.*, 2016, **15**, 691–692.

8 J. H. Yang, H. L. Yip and A. K. Y. Jen, *Adv. Energy Mater.*, 2013, **3**, 549–565.

9 Y. C. Lan, A. J. Minnich, G. Chen and Z. F. Ren, *Adv. Funct. Mater.*, 2009, **20**, 357–376.

10 Z. H. Ge, L. D. Zhao, D. Wu, X. Y. Liu, B. P. Zhang, J. F. Li and J. Q. He, *Mater. Today*, 2016, **19**, 227–239.

11 B. C. Sales, D. Mandrus and R. K. Williams, *Science*, 1996, **272**, 1325–1328.

12 X. Shi, J. Yang, J. R. Salvador, M. F. Chi, J. Y. Cho, H. Wang, S. Q. Bai, J. H. Yang, W. Q. Zhang and L. D. Chen, *J. Am. Chem. Soc.*, 2011, **133**, 7837–7846.

13 G. S. Nolas, J. L. Cohn, G. A. Slack and S. B. Schujman, *Appl. Phys. Lett.*, 1998, **73**, 178–180.

14 X. Shi, J. Yang, S. Q. Bai, J. H. Yang, H. Wang, M. F. Chi, J. R. Salvador, W. Q. Zhang, L. D. Chen and W. Wong-Ng, *Adv. Funct. Mater.*, 2010, **20**, 755–763.

15 M. Christensen, S. Johnsen and B. B. Iversen, *Dalton Trans.*, 2010, **39**, 978–992.

16 J. W. Zhang, R. H. Liu, N. Cheng, Y. B. Zhang, J. H. Yang, C. Uher, X. Shi, L. D. Chen and W. Q. Zhang, *Adv. Mater.*, 2014, **26**, 3848–3853.

17 T. Plirdpring, K. Kurosaki, A. Kosuga, T. Day, S. Firdosy, V. Ravi, G. J. Snyder, A. Harnwunggmoung, T. Sugahara, Y. Ohishi, H. Muta and S. Yamanaka, *Adv. Mater.*, 2012, **24**, 3622–3626.

18 H. L. Liu, X. Shi, F. F. Xu, L. L. Zhang, W. Q. Zhang, L. D. Chen, Q. Li, C. Uher, T. Day and G. J. Snyder, *Nat. Mater.*, 2012, **11**, 422–425.

19 Y. He, T. Day, T. S. Zhang, H. L. Liu, X. Shi, L. D. Chen and G. J. Snyder, *Adv. Mater.*, 2014, **26**, 3974–3978.

20 G. A. Slack, *CRC Handbook of Thermoelectrics*, CRC Press, Boca Raton, 1995.

21 Y. He, T. S. Zhang, X. Shi, S. H. Wei and L. D. Chen, *NPG Asia Mater.*, 2015, **7**, e210.

22 S. Ballikaya, H. Chi, J. R. Salvador and C. Uher, *J. Mater. Chem. A*, 2013, **1**, 12478–12484.

23 S. Ishiwata, Y. Shiomi, J. S. Lee, M. S. Bahramy, T. Suzuki, M. Uchida, R. Arita, Y. Taguchi and Y. Tokura, *Nat. Mater.*, 2013, **12**, 512–517.

24 G. C. Tewari, M. Karppinen and A. K. Rastogi, *J. Solid State Chem.*, 2013, **198**, 108–113.

25 S. Bhattacharya, R. Basu, R. Bhatt, S. Pitale, A. Singh, D. K. Aswal, S. K. Gupta, M. Navaneethan and Y. Hayakawa, *J. Mater. Chem. A*, 2013, **1**, 11289–11294.

26 X. Zhang, C. L. Zhang, S. Q. Lin, H. Lu, Y. Z. Pei and S. Jia, *J. Appl. Phys.*, 2016, **119**, 135101.

27 A. Charoenphakdee, K. Kurosaki, H. Muta, M. Uno and S. Yamanaka, *Phys. Status Solidi RRL*, 2008, **2**, 65–67.

28 T. J. Zhu, S. N. Zhang, S. H. Yang and X. B. Zhao, *Phys. Status Solidi RRL*, 2010, **4**, 317–319.

29 A. Charoenphakdee, K. Kurosaki, H. Muta, M. Uno and S. Yamanaka, *Jpn. J. Appl. Phys.*, 2009, **48**, 011603.

30 L. Li, Y. Liu, J. Y. Dai, A. J. Hong, M. Zeng, Z. B. Yan, J. Xu, D. Zhang, D. Shan, S. L. Liu, Z. F. Ren and J. M. Liu, *J. Mater. Chem. C*, 2016, **4**, 5806–5813.

31 W. Li, S. Q. Lin, B. H. Ge, J. Yang, W. Q. Zhang and Y. Z. Pei, *Adv. Sci.*, 2016, **7**, 1600196.

32 W. F. Kuhs, R. Nitsche and K. Scheunemann, *Mater. Res. Bull.*, 1979, **14**, 241–248.

33 E. Gaudin, F. Taulelle, F. Boucher and M. Evain, *J. Chim. Phys. Phys.-Chim. Biol.*, 1998, **95**, 295–301.

34 M. H. Chen, X. S. Yin, M. V. Reddy and S. Adams, *J. Mater. Chem. A*, 2015, **3**, 10698–10702.

35 K. S. Weldert, W. G. Zeier, T. W. Day, M. Panthofer, G. J. Snyder and W. Tremel, *J. Am. Chem. Soc.*, 2014, **136**, 1203512040.

36 Oxford Diffraction, *CrysAlis Pro*, Oxford Diffraction Ltd, England, 2006.

37 O. V. Dolomanov, L. J. Bourhis, R. J. Cildea, J. A. K. Howard and H. Puschmann, *J. Appl. Crystallogr.*, 2009, **42**, 339–341.

38 L. Farrugia, *J. Appl. Crystallogr.*, 1999, **32**, 837–838.

39 J. Rodríguez-Carvajal, *Phys. B*, 1993, **192**, 55–69.

40 R. M. Matin, *Electronic Structure: Basic Theory and Practical Methods*, Cambridge University Press, Cambridge, 2004.

41 A. Togo, F. Oba and I. Tanaka, *Phys. Rev. B: Condens. Matter Mater. Phys.*, 2008, **78**, 134106.

42 S. Jaulmes, M. Julien-Pouzol, P. Laruelle and J. Rivet, *Acta Crystallogr., Sect. C: Cryst. Struct. Commun.*, 1991, **47**, 1799–1803.

43 G. Kresse and J. Furthmüller, *Comput. Mater. Sci.*, 1996, **6**, 15–50.

44 Y. B. Zhang, X. Yuan, X. D. Sun, B. C. Shih, P. H. Zhang and W. Q. Zhang, *Phys. Rev. B: Condens. Matter Mater. Phys.*, 2011, **84**, 075127.

45 F. Boucher, M. Evain and R. Brec, *J. Solid State Chem.*, 1993, **107**, 332–346.

46 H. Wada, A. Onoda, A. Ishii, A. Sato, A. Tansho and N. Iyi, *J. Alloys Compd.*, 2004, **383**, 144–147.

47 T. Nilges and A. Pfitzner, *Z. Kristallogr.*, 2005, **220**, 281–294.

48 E. A. Davis and N. F. Mott, *Philos. Mag.*, 1970, **22**, 903–922.

49 R. López and R. Gómez, *J. Sol-Gel Sci. Technol.*, 2012, **61**, 1–7.

50 J. J. Shen, T. J. Zhu, X. B. Zhao, S. N. Zhang, S. H. Yang and Z. Z. Yin, *Energy Environ. Sci.*, 2010, **3**, 1519–1523.

51 P. F. Qiu, T. S. Zhang, Y. T. Qiu, X. Shi and L. D. Chen, *Energy Environ. Sci.*, 2014, **7**, 4000–4006.

52 G. A. Slack, *Solid State Phys.*, 1979, **34**, 1–71.

53 L. D. Zhao, S. H. Lo, Y. S. Zhang, H. Sun, G. J. Tan, C. Uher, C. Wolverton, V. P. Dravid and M. G. Kanatzidis, *Nature*, 2014, **508**, 373–377.

54 M. D. Nielsen, V. Ozolins and J. P. Heremans, *Energy Environ. Sci.*, 2013, **6**, 570–578.

55 I. K. Dimitrov, M. E. Manley, S. M. Shapiro, J. Yang, W. Zhang, L. D. Chen, Q. Jie, G. Ehlers, A. Podlesnyak, J. Camacho and Q. Li, *Phys. Rev. B: Condens. Matter Mater. Phys.*, 2010, **82**, 174301.

56 V. Keppens, D. Mandrus, B. C. Sales, B. C. Chakoumakos, P. Dai, R. Coldea, M. B. Maple, D. A. Gajewski, E. J. Freeman and S. Bennington, *Nature*, 1998, **395**, 876–878.

57 W. Schnelle, A. Leithe-Jasper, H. Rosner, R. Cardoso-Gil, R. Gumeniuk, D. Trots, J. A. Mydosh and Y. Grin, *Phys. Rev. B: Condens. Matter Mater. Phys.*, 2008, **77**, 094421.

58 K. Suekuni, M. A. Avila, K. Umeo and T. Takabatake, *Phys. Rev. B: Condens. Matter Mater. Phys.*, 2007, **75**, 195210.

59 H. L. Liu, J. Yang, X. Shi, S. A. Danilkin, D. H. Yu, C. Wang, W. Q. Zhang and L. D. Chen, *J. Materiomics*, 2016, **2**, 187–195.

60 J. Callaway, *Phys. Rev.*, 1959, **113**, 1046.

61 J. Yang, D. Morelli, G. Meisner, W. Chen, J. Dyck and C. Uher, *Phys. Rev. B: Condens. Matter Mater. Phys.*, 2003, **67**, 165207.

62 T. J. Zhu, C. G. Fu, H. H. Xie, Y. T. Liu, B. Feng, J. Xie and X. B. Zhao, *Europhys. Lett.*, 2013, **104**, 46003.

63 G. Dennler, R. Chmielowski, S. Jacob, F. Capet, P. Roussel, S. Zastrow, K. Nielsch, I. Opahle and G. K. H. Madsen, *Adv. Energy Mater.*, 2014, **4**, 1301581.

64 D. R. Brown, T. Day, T. Caillat and G. J. Snyder, *J. Electron. Mater.*, 2013, **42**, 2014–2019.